

UNIVERSITY of CALIFORNIA
SANTA CRUZ

**A PROTON COMPUTED TOMOGRAPHY HEAD SCANNER DATA
ANALYSIS**

A thesis submitted in partial satisfaction of the
requirements for the degree of

BACHELOR OF SCIENCE

in

PHYSICS

by

Evan C. Harvey

6 June 2016

The thesis of Evan C. Harvey is approved by:

Professor Robert P. Johnson
Advisor

Professor Adriane Steinacker
Theses Coordinator

Professor Robert P. Johnson
Chair, Department of Physics

Copyright © by

Evan C. Harvey

2016

Abstract

A Proton Computed Tomography Head Scanner Data Analysis

by

Evan C. Harvey

I present the relevant framework of characterizing ionizing radiation, a description of the apparatus of a Proton Computed Tomography (pCT) head scanner and how it can potentially improve the accuracy of proton radiation therapy. The data acquisition system (DAQ) of the pCT scanner registers detected protons in its energy detectors as events. I have defined 6 sequential steps that the preprocessing code uses to evaluate these events from the DAQ as well as an example of a beam test run file being processed by these steps. Via the investigation of a beam test run taken while the energy detectors were warming up compared with a beam test run taken while the energy detectors were in essentially systematic thermal equilibrium, it appears the calorimeter does have a temperature dependence. After creating artificial gaps in the tracking board of the pCT scanner apparatus that originally contained detected hits, I have found that the track reconstruction algorithm in the preprocessing code is able to recover the detected hit's position within a factor of three of its original position's uncertainty, note the reconstruction code has been updated since this analysis so this result may be different now. By making a square centimeter fluence constraint extrapolated to the center point of where a phantom is rotated and scanned, I was able to calculate an analytical approximation to a water equivalent absorbed dose of about 1.13 mGy for a 6 minute scan. An ionization chamber located within the same vicinity of the phantom region I calculated a dose for measured a dose of about 1.40 mGy, I believe the discrepancy between this measurement and my calculated value is mostly due to the fact that I neglected scattering events and assumed straight lined trajectories of the protons through my fluence constraint when most likely many of these proton trajectories may have been curved.

Contents

List of Figures	v
List of Tables	vii
Dedication	viii
Acknowledgements	ix
1 Introduction	1
1.1 Characterizing Ionization	2
1.2 Proton Radiation Therapy	4
2 The Apparatus	7
2.1 Tracking Board System	8
2.2 5-Stage Energy Detector	9
3 Preprocessing The Data	10
3.1 Step 1: Not Enough Hits	11
3.2 Step 2: Too Many Hits	12
3.3 Step 3: At Least One 2D Track	13
3.4 Step 4: Displacement Test	14
3.5 Step 5: At Least One T and V Super Track	15
3.6 Step 6: Too Many Super Tracks	16
3.7 A Step Distribution	16
4 Temperature Dependence of 5-Stage Energy Detector	18
5 Efficiency of the Track Reconstruction Algorithm	23
6 Analytic Determination of Dose	29
7 Conclusion	33
A The Possibilities of Step 1	34
B Justifying $\sqrt{12}$	35
Bibliography	37

List of Figures

1.1	This figure displays the most important pathways for growth control and cell cycle regulation [1].	1
1.2	This figure displays an artist's depiction of an atom's collisional interaction within a medium, I like to think of the blue/purple lines as perturbed electromagnetic field lines of the incident particle although I am not sure what exact physics this artist was trying to depict (image sourced from [3]).	4
1.3	This figure displays a conceptualization to the idea of a patient not experiencing an exit dose from targeted proton therapy (image sourced from [4]).	5
2.1	This figure [3] displays the important pieces of the pCT scanner apparatus that will be in constant reference throughout this thesis (excluding the Rotation Stage). . . .	7
2.2	This figure displays a diagram of the tracking board system of the pCT scanner, the image (still a work in progress) was designed by myself, note direction V points into the page.	9
3.1	This figure displays an event that has failed to pass through Step 1 because there are no hits in the third tracker board.	11
3.2	This figure displays an event that has failed to pass through Step 2 because there are three hits in the third tracker board's T layer.	12
3.3	This figure displays an event that has failed to pass through Step 3 because there is a missing hit in the first tracking board's T layer.	13
3.4	This figure displays an event that is being checked by Step 4 for the trajectory created by the T layer hits.	14
3.5	This figure is a pie chart displaying how many events a sequential step rejects relative to another step.	17
4.1	STEP 1: This is an example of a histogram displaying an energy detector's (channel 4 in this picture) pulse heights. I look at these histograms for all channels 0-4 for every run I am going to use in my final graph.	19
4.2	STEP 2: This is a gaussian fit being applied to the most prominent (single proton) peak of the histogram from the last slide. I write down the displayed mean/sigma values of this gaussian fit.	19
4.3	STEP 3: This is the scanned image of the water phantom taken from the March beam test. I only used both side areas where the protons completely miss the phantom for the analysis.	20
4.4	STEP 4/finale: With the December test on the left and the March test on the right, we can see the energy detectors pulse heights change systematically over time for the December test, which is when the machine was heating up as the test was running. .	21

4.5	STEP 4/finale: Notice the slopes for the March Beam Test are extremely close to zero or contain zero in their interval of error relative to the slopes for the December Beam Test. The non-small magnitude in all the slopes for the channels in the December Beam Test indicate there is a noticeable change in the pulse height over time as the machine is warming up	21
5.1	This figure displays the first T layer and the relative orientation of the artificial gaps I created.	24
5.2	These are the raw T-Board layer 0 distributions, as you can see, on the left is the artificial gap I created, and on the right is the successful work of the geometric algorithm generating artificial hits for this gap; effectively filling it. Being that this sensor board is on a far side not as close to the incoming beam, there is less hits to work with so the artificial gap in the position distribution is noticeable smaller..... notice how the sensors are flipped, the reason for this is beyond my knowledge.	25
5.3	These are the raw T-Board layer 0 distributions for the specific gap regions. On the left is the real hit distribution before it was removed to create an artificial gap and on the right is the recovered/artificial hit distribution created by the geometric algorithm. generating artificial hits for this gap; effectively filling it.	26
5.4	This figure displays the resulting distribution of taking the difference between both distributions displayed in Fig. 5.3	27
5.5	This figure displays the resulting σ_{reco} 's I found for every T board's (Layer 0) sensor's created artificial gap as well as σ_{real} for convenient visual comparison.	28
6.1	This figure displays the path of a single accelerated proton that travels through my square cm constraint as well as the amount of energy this proton loses/deposits through the various mediums of the pCT scanner apparatus.	31

List of Tables

3.1	Rejected Event Tracker updated after Step 1.	12
3.2	Rejected Event Tracker updated after Step 2.	13
3.3	Rejected Event Tracker updated after Step 3.	14
3.4	Rejected Event Tracker updated after Step 4.	15
3.5	Rejected Event Tracker updated after Step 5.	15
3.6	Rejected Event Tracker updated after Step 6.	16
A.1	This table displays every possible case of tracker board hit combination that can cause an event to fail Step 1.	34

Dedicated to the atomic landscape around me.

Acknowledgements

I want to thank my research advisors Robert Johnson and Hartmut Sadrozinski for their excellent guidance in my exploration of the field of proton Computed Tomography. I also would like to thank all of my family and friends for being in my life but most importantly, my father David Harvey, who endured so much to get me where I am today.

1 Introduction

Cancer has plagued the biological fragility of the human body for countless generations. To this day a complete cure is being feverishly pursued, but this naturally leads to the question of why hasn't cancer been cured yet? While I could answer this question by attempting to cover the enormous amount of complexity involved in cellular interactions and how they give rise to cancerous tissue, I will instead trouble the reader with Fig. 1.1.

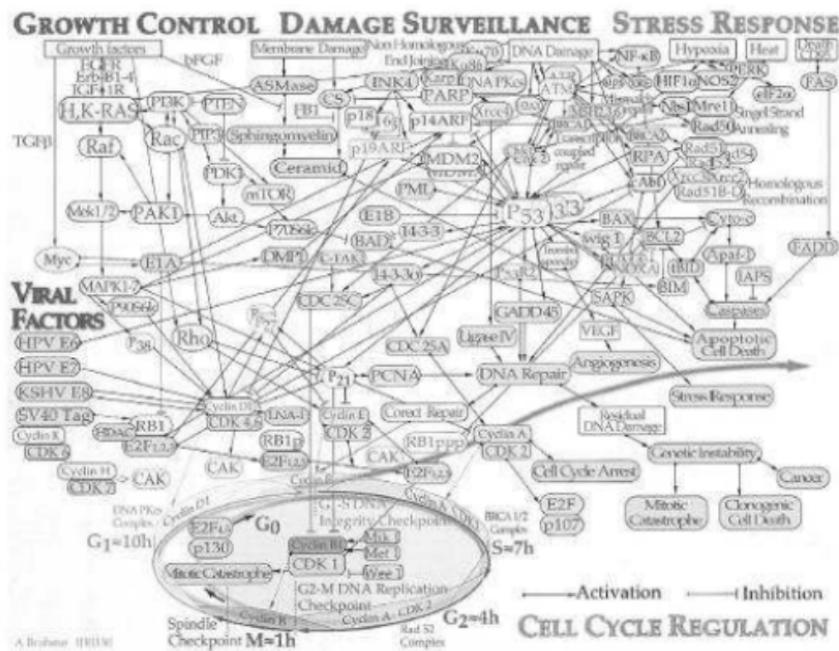


Figure 1.1: This figure displays the most important pathways for growth control and cell cycle regulation [1].

To make matters worse, Fig. 1.1 is just a simplification to the complete picture of cancer

and the causes. Although certain physical phenomena can definitely increase your chance of developing cancer, a direct cause and effect just simply hasn't been established yet. Some people who live as healthy lives as possible can go on to develop cancer, possibly due to their genetics or the very stochastic nature of DNA mutations causing cancer development. Throughout the evolution of science and medicine, various methods of treatment have been developed to combat and destroy cancer. One category of treatment known as External Beam Radiation Therapy (EBRT) involves methodically shooting charged particles, neutrons, or photons into the human body to effectively destroy cancerous cell tissue. Proton radiation therapy is the type of EBRT that involves using protons for the desired ionization. The more a proton slows down from its acceleration per centimeter of travel, the more radiation it deposits. The consequence of this process means that an accelerated proton will deposit relatively a significant amount of its energy in the region where it stops. This deposited energy can ionize the atoms of the medium within the local vicinity of the decelerating proton.

1.1 Characterizing Ionization

When an atom is ionized an electron is stripped from its potential well. This process leaves an electron shell vacancy within the atom. The 8 dominant ways of electron shell vacancy production are pair annihilation, Compton Effect, Auger Effect, columbic interactions, triplet production, internal conversion, photoelectric effect, and electron capture [2]. A key thing to note here is that these 8 processes can trigger each other, so characterizing what type of interaction is responsible for an electron shell vacancy production can become a seemingly fractal mess very quickly. For example, let's say an accelerated electron incident on a medium has a columbic interaction with a bound electron of that medium effectively ionizing it and then that freed electron has bremsstrahlung radiation (from being slowed down in the medium) producing photons which may cause photoelectric/Compton interactions (possibly pair and triplet production but let's restrict ourselves just a little as the bremsstrahlung radiation required for this would be quite relatively high in energy)

within the medium. This freed electron could also cause an auger interaction via another bound electron (to the same atom the ionized electron was freed from) falling into it's vacant orbital shell emitting a photon that could knock out another electron bound from that same atom, and that newly ionized electron could... well I think you you get the picture! The question that naturally arises is how do you define the probabilities/weighted averages of how much each interaction is responsible for an ionization event. Surely these interactions must be mathematically well defined if this is all happening in the human body? The answer to this question is extensively covered in advanced radiation physics and will not be of a concern in this thesis, but I did bring up this all up for a reason.

Within the process of proton radiation therapy, coulombic interactions are the main interaction responsible for the ionization of a medium subjected to incident accelerated protons. However, some of the other 8 electron shell vacancy production processes may arise as well during a proton radiation interaction with a medium, so I believe it is worthwhile for the reader to be aware of the fractal nature of what's *really going on* as far as the physics of ionization is concerned. I will end this brief digression on radiation physics with an artist's depiction of the beauty of the complex nature of an atomic collision displayed in Fig. 1.2.

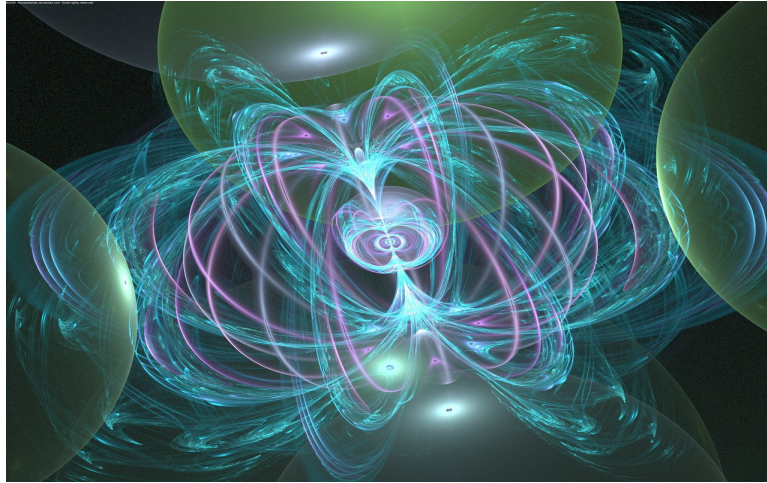


Figure 1.2: This figure displays an artist's depiction of an atom's collisional interaction within a medium, I like to think of the blue/purple lines as perturbed electromagnetic field lines of the incident particle although I am not sure what exact physics this artist was trying to depict (image sourced from [3]).

When an electron is ionized from an atom, it can go on to interact with nearby atoms as was previously discussed. Ideally, the DNA of cancerous cell tissue is at the forefront of the medium being subjected to the ionization caused by decelerating protons. Let's explore why this is so.

1.2 Proton Radiation Therapy

In targeted proton therapy, the accelerated incident proton ideally stops at the tumor within a patient, and there is no exit dose out of the body unlike conventional radiation therapy. The contrast between the two is displayed in Fig. 1.3.

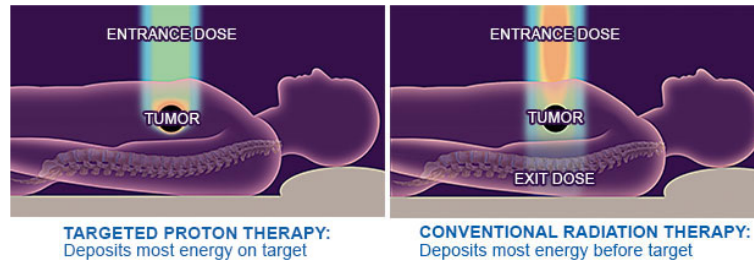


Figure 1.3: This figure displays a conceptualization to the idea of a patient not experiencing an exit dose from targeted proton therapy (image sourced from [4]).

After measuring the stopping power of the relevant incident tissue to predict the proton's range of ionization influence, calibrating the kinetic energy of the proton to deposit most of its energy in a cancerous cell tissue region while depositing a relatively negligible (biologically safe) amount of energy to the surrounding noncancerous cell region is the name of the game in proton radiation therapy. The idea of using protons in medical treatment was first suggested in 1946 by physicist Robert R. Wilson, Ph.D. The first attempts to use proton radiation to treat patients began in the 1950s in nuclear physics research facilities, but applications were limited to few areas of the body [5]. As of today, proton radiation therapy is much more commonplace, and the developmental research for its improvement with proton Computed Tomography (pCT) will be the entire emphasis of this thesis.

For any EBRT, one needs a distribution of the targeted material's electron density; an image. Currently, images for targeted proton radiation treatment are taken with X-ray Computed Tomography (X-ray CT). When a collection of X-rays pass through the body they can have different attenuations with respect to each other depending on the medium's local density and material type (with respect to nucleic charge/atomic number configuration) that each X-ray traverses through. When these attenuated X-rays are analyzed, a Hounsfield unit is prescribed as a proportionality to the degree of x-ray attenuation and it is allocated to each pixel to show the image that represents the density of the tissue. For targeted proton therapy, these Hounsfield values must be converted to proton stopping power. The idea of pCT is to measure directly a 3D map of proton stopping

power within a patient in order to eliminate the step of converting Hounsfield values to proton stopping power, which has been found to introduce proton range errors of 2-3%. These errors have to do with the fact that X-ray interactions depend on both electron density and atomic number Z in a complicated way while proton stopping power has most of its dependence on just the electron density, these differing dependencies lead to ambiguities in the transformation from Hounsfield values to relative stopping power values. The pCT scanning system uses protons in transmission such that the Bragg peak is deposited in a downstream calorimeter or range detector, from which the residual energy is calibrated to the proton's water equivalent path length. During image reconstruction, a 3D image is reconstructed such that the voxels are rendered in terms of proton relative stopping power.

Even though the history of proton radiography and tomography goes back half a century, no clinical system yet exists for pCT. [6]. Like any device that is involved with ionizing radiation to the human body, there has to be a rigorous screening process of tests before clinical trials. Within these tests, there are methods of data analysis to understand the efficiency and accuracy of the data acquisition system (DAQ) for the pCT scanner. This thesis will explore some of these methods. Before this is done, we need to understand the apparatus of the pCT head scanner itself.

2 The Apparatus

The relevant framework of the pCT scanning system is displayed in Fig. 2.1.

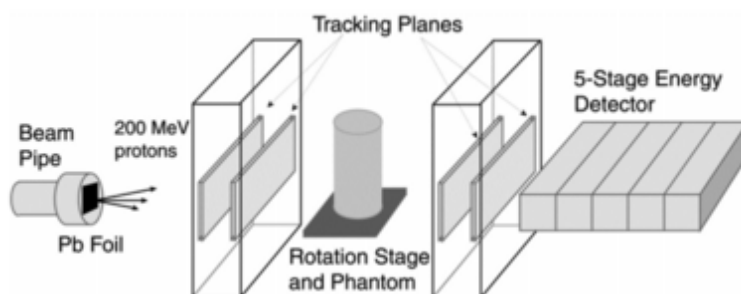


Figure 2.1: This figure [3] displays the important pieces of the pCT scanner apparatus that will be in constant reference throughout this thesis (excluding the Rotation Stage).

As protons exit the beam pipe from an the synchrotron at Loma Linda University, they first are scattered by a lead foil to exhibit a divergence of the beam into a cone-like shape. At the Chicago Proton Center (which is where tests are now being performed at instead of Loma Linda) a lead foil is not used. The beam (from a cyclotron instead of a synchrotron) is wobbled back and forth across the aperture by magnets, sometimes it is made a bit wider by inserting a tantalum foil into the beam. From this point on we will follow the path of a single proton that makes it all the way to the calorimeter (some protons don't make it to the calorimeter for various reasons). An incident proton from the beam pipe will initially interact with the front telescope which is a component of the tracking board system.

2.1 Tracking Board System

The tracking board system during data analysis is usually described/categorized as a front telescope and a back telescope. The front telescope consists of the first two tracking boards an incident proton will interact with and the back telescope consists of the last two tracking boards a proton will interact with after it has passed through a phantom (collection of matter subjected to the scan for imaging). I will denote the four tracking boards from closest to beam pipe to closest to the calorimeter as boards 0, 1, 2, 3 respectively throughout this thesis. Each board contains two layers denoted as T or V where T corresponds to a horizontal coordinate and V corresponds to a vertical coordinate. The T/V layers comprise of silicon strip detectors that can detect an incident proton passing through them. Each T layer and V layer is one board upon which are mounted 4 silicon-strip detectors (wafers). On V layers the strips are horizontal, and strips on pairs of detectors are ganged together while on T layers the strips are vertical and there is no ganging together. Thus there are apparent “gaps” in the tracking boards. While V layers have just as many gaps as T layers, the difference is that the gaps are perpendicular to the strips in V layers, so they are not so obvious in the data. For purposes of my analysis, Fig. 2.2 displays a closer look at this tracking board system as well as the designated chip addresses within the boards and how I visualize the gaps.

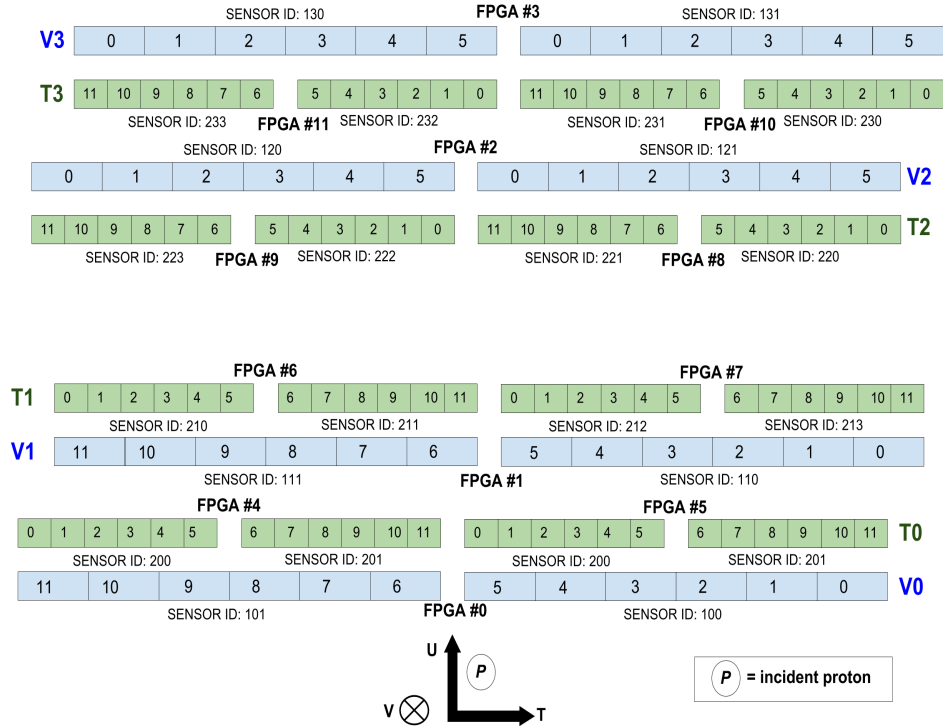


Figure 2.2: This figure displays a diagram of the tracking board system of the pCT scanner, the image (still a work in progress) was designed by myself, note direction V points into the page.

2.2 5-Stage Energy Detector

After accelerated protons pass through a phantom and the final two tracking boards (2 and 3), they are ideally “caught” inside the calorimeter. The calorimeter of the pCT system is an energy detector divided into five stages. As an accelerated proton stops somewhere within these five stages, their deposited energy can be measured and mathematically used to infer the energy loss they exhibited while traveling through the phantom being scanned. I will sometimes refer to these stages as channels throughout this thesis. The channels/stages consist of plastic scintillators, 5.1 cm thick segments of UPS-923A poly-styrene-based scintillator read out by R3318 Hamamatsu photo-multiplier tubes [6].

3 Preprocessing The Data

During a scan, the arrays of silicon strip detectors within the tracking boards of the pCT scanner detect a “hit” when a proton passes through them. The collection of hits between the tracking boards can give geometrical information on a proton’s trajectory. Protons can have various interactions when traveling through matter (relevant matter includes the phantom being scanned, the tracking boards themselves, etc.). Some of these interactions such as elastic and inelastic scattering with the atoms of the traversed medium can compromise the proton from being able to be used in image reconstruction. The events from the DAQ that contain unfavorable proton interactions are ideally removed when a ”preprocessing code” is ran on a beam test run file containing information from the DAQ. If the preprocessing code fails to assign exactly one “super track” to an event, the event is deemed no good and rejected for potential use in image reconstruction. An event gets assigned exactly one super track if it passes all the various constraints from the algorithms of the preprocessing code. I have categorized the preprocessing code to have essentially 6 sequential cutting steps (constraints) on the data. If an event passes through these 6 cuts, it gets assigned exactly one super track. Let’s examine these sequential cutting steps and their influence on an example beam test run file. The one to be used is an empty run (no phantom) taken from a beam test that was done in May 2015. It contains 11,519,824 events. For convenience, I will denote this file as File P and I will display a File P event tracker through every step to keep track of how many events are rejected from each cut. Every diagram for each step indicates one single proton track because that is what an ”event” is **supposed** to represent (a lot of these cuts are done because the event’s tracking

board contradicts the assumption of a single proton track).

3.1 Step 1: Not Enough Hits

An event will not pass through step 1 if it does not have enough hits in the tracking board layers. This could happen if a proton experiences scattering along its trajectory, goes through the tracking board gaps, or goes through a "hot strip" detector where the detector hasn't reset yet from another proton it previously detected. The constraint defining "not enough hits" is the following: if a TV layer pair contains no hits or every TV layer pair contains only one hit (so entire event has four tracker board hits), the event is rejected.

Being that there are 2 layers (T and V) per tracking board and that there are four tracking boards, there are $2^4 = 16$ cases where an event will fail this cut. The amount of events rejected for each of these 16 cases (and the description of these cases) for File P is displayed in Table blah in appendix bleh., these ways are described in Table 1. One example of these 16 cases is displayed in Fig. 3.1 for a conceptualization.

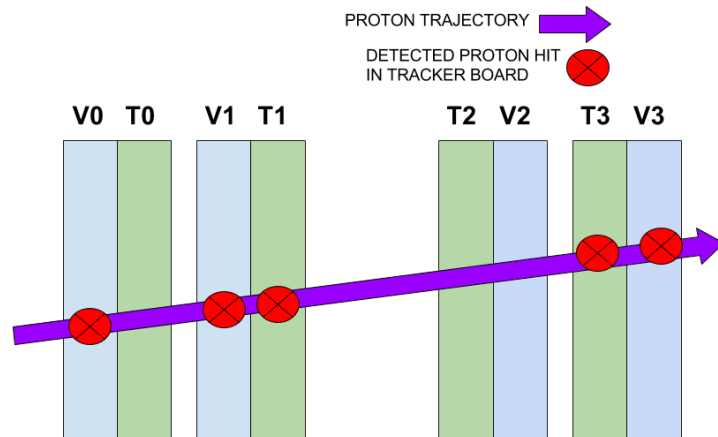


Figure 3.1: This figure displays an event that has failed to pass through Step 1 because there are no hits in the third tracker board.

In Fig. 3.1 the third tracking board does not detect the incident proton's presence in either

of its layers, so this is why the example event fails to pass step 1.

After every event for File P is ran through step 1 our rejected event tracker is updated in Table 3.1.

Table 3.1: Rejected Event Tracker updated after Step 1.

	EVENTS REJECTED PER STEP	TOTAL EVENTS LEFT	PERCENTAGE OF TOTAL EVENTS CUT PER STEP
STEP 1	-766,922	10,752,904	-6.66%

So, 6.66% of the total events detected for File P are rejected as potential candidates for image reconstruction because they failed to pass through Step 1.

3.2 Step 2: Too Many Hits

An event will not pass through Step 2 if it contains three or more hits in any respective tracking board T or V layer. An example of an event failing this step is displayed in Fig 3.2.

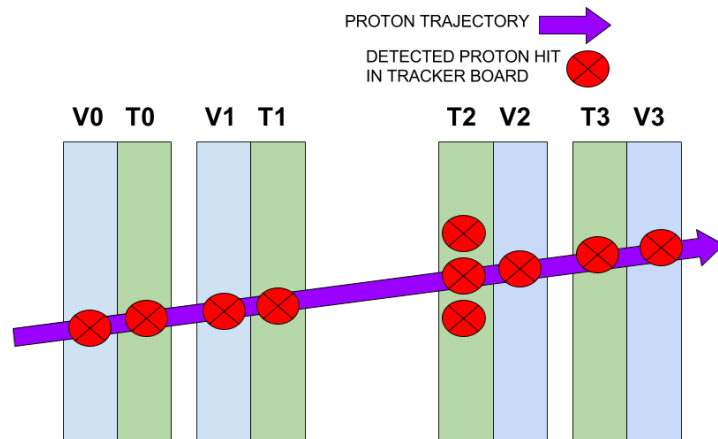


Figure 3.2: This figure displays an event that has failed to pass through Step 2 because there are three hits in the third tracker board's T layer.

After every event for File P is ran through step 2 our rejected event tracker is updated in

Table 3.2.

Table 3.2: Rejected Event Tracker updated after Step 2.

	EVENTS REJECTED PER STEP	TOTAL EVENTS LEFT	PERCENTAGE OF TOTAL EVENTS CUT PER STEP
STEP 1	-766,922	10,752,904	-6.66%
STEP 2	-85,582	10,667,320	-0.74%

So, 0.74% of the total events detected for File P are rejected as potential candidates for image reconstruction because they failed to pass through Step 2.

3.3 Step 3: At Least One 2D Track

The event displayed in Fig. 3.3 passes Steps 1 and 2, but it meets its fate of rejection at Step 3 since it is missing a hit in the first tracking board's T layer, thus a complete track has been unable to be reconstructed.

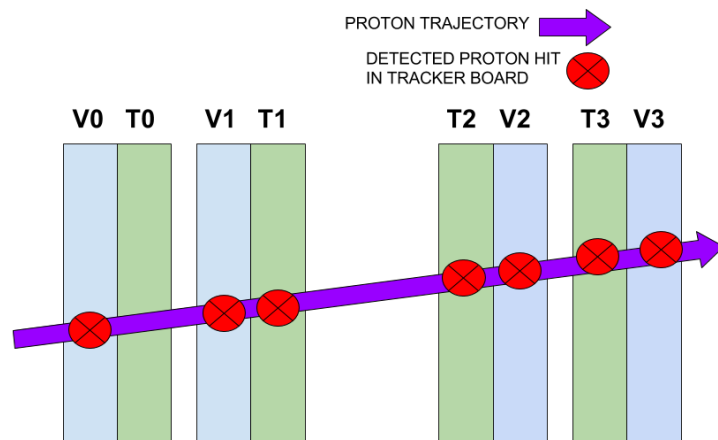


Figure 3.3: This figure displays an event that has failed to pass through Step 3 because there is a missing hit in the first tracking board's T layer.

The reason my title for Step 3 includes "At Least One" is because in Step 2 I rejected events that had 3 hits in a single layer, but I said nothing about 2 hits (notice how Fig. 3.3 does

not have two hits in any layer, only one). After every event for File P is ran through Step 3 our rejected event tracker is updated in Table 3.3.

Table 3.3: Rejected Event Tracker updated after Step 3.

	EVENTS REJECTED PER STEP	TOTAL EVENTS LEFT	PERCENTAGE OF TOTAL EVENTS CUT PER STEP
STEP 1	-766,922	10,752,904	-6.66%
STEP 2	-85,582	10,667,320	-0.74%
STEP 3	-823162	9,844,158	-7.15%

So, 7.15% of the total events detected for File P are rejected as potential candidates for image reconstruction because they failed to pass through Step 3.

3.4 Step 4: Displacement Test

For Step 4, the tracks created by the V layer hits and the tracks created by the T layer hits are independently looked at. For either one, a track made in the front telescope and a track made in the back telescope are projected to the center of the tracking board system, if the perpendicular distance between each track is larger than what I will define as the distance r , the event is rejected.

An example of this process is displayed in Fig. 3.4.

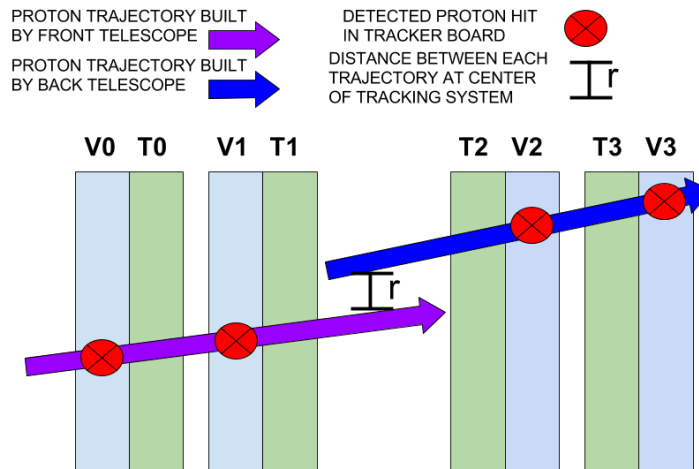


Figure 3.4: This figure displays an event that is being checked by Step 4 for the trajectory created by the T layer hits.

If the event passes the displayed test in Fig. 3.4 (distance between two tracks is less than r), that event will be assigned a T Super Track. Likewise, if that event passed the same test displayed in Fig. 3.4 but for hits in the V layer instead, it would be assigned a V Super Track. After every event for File P is ran through Step 4 our rejected event tracker is updated in Table 4.

Table 3.4: Rejected Event Tracker updated after Step 4.

	EVENTS REJECTED PER STEP	TOTAL EVENTS LEFT	PERCENTAGE OF TOTAL EVENTS CUT PER STEP
STEP 1	-766,922	10,752,904	-6.66%
STEP 2	-85,582	10,667,320	-0.74%
STEP 3	-823162	9,844,158	-7.15%
STEP 4	-564010	9,280,148	-4.90%

So, 4.90% of the total events detected for File P are rejected as potential candidates for image reconstruction because they failed to pass through Step 4.

3.5 Step 5: At Least One T and V Super Track

For an event to pass Step 5, it has to be assigned at least one T Super Track and one V Super Track (as defined in Step 4). After every event for File P is ran through Step 5 our rejected event tracker is updated in Table 3.5.

Table 3.5: Rejected Event Tracker updated after Step 5.

	EVENTS REJECTED PER STEP	TOTAL EVENTS LEFT	PERCENTAGE OF TOTAL EVENTS CUT PER STEP
STEP 1	-766,922	10,752,904	-6.66%
STEP 2	-85,582	10,667,320	-0.74%
STEP 3	-823162	9,844,158	-7.15%
STEP 4	-564010	9,280,148	-4.90%
STEP 5	-895,494	8,384,654	-7.77%

So, 7.77% of the total events detected for File P are rejected as potential candidates for image reconstruction because they failed to pass through Step 5.

3.6 Step 6: Too Many Super Tracks

For an event to pass Step 6, it must have exactly one super track, which means it must have exactly one T Super Track and one V Super Track. After every event for File P is ran through step 6 our rejected event tracker is updated in Table 3.6.

Table 3.6: Rejected Event Tracker updated after Step 6.

	EVENTS REJECTED PER STEP	TOTAL EVENTS LEFT	PERCENTAGE OF TOTAL EVENTS CUT PER STEP
STEP 1	-766,922	10,752,904	-6.66%
STEP 2	-85,582	10,667,320	-0.74%
STEP 3	-823162	9,844,158	-7.15%
STEP 4	-564010	9,280,148	-4.90%
STEP 5	-895,494	8,384,654	-7.77%
STEP 6	-620567	7,804,087	-5.39%

So, 5.39% of the total events detected for File P are rejected as potential candidates for image reconstruction because they failed to pass through Step 6.

3.7 A Step Distribution

File P has now finished running through the sequential steps I have defined for the preprocessing code, I can now examine some properties of the preprocessing code via the results of Rejected Event Tracker table I kept updating. So File P started with 11,519,824 events and 7,804,087 of those events made it through every step of the preprocessing code which implies that about 32% of File P's recorded events are rejected as potential candidates for image reconstruction. Within this 32%, Fig. 3.5 displays the amount of influence each step holds among the total number of rejected events for File P.

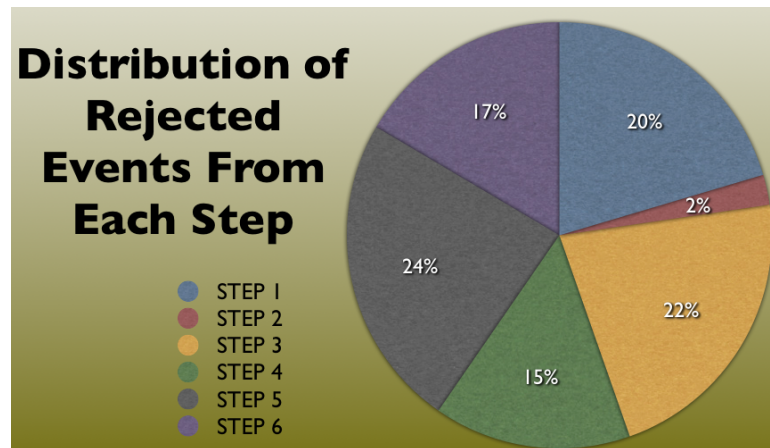


Figure 3.5: This figure is a pie chart displaying how many events a sequential step rejects relative to another step.

Notice Step 5 rejects the most events and Step 2 rejects the least number of events. Now, Fig. 3.5 may give different results for different beam test runs. It is worthy to mention that File P was for a run with no phantom. I chose it for a simple example to explain how the preprocessing code evaluates a beam test run file.

4 Temperature Dependence of 5-Stage Energy Detector

When protons stop in the various scintillator stages and deposit their residual energy, the R3318 Hamamatsu photo-multiplier tubes mentioned in section 2.2 detect the scintillation light corresponding to the proton's energy deposition. After the pCT scanner is turned on for initial operation, it will warm up from the heat dissipation of its internal electronics as the DAQ responds to an incident proton beam. To investigate if this temperature increase is affecting the output of the photomultiplier tubes detecting the scintillation light (which can alter the readings of an incident proton's residual energy), I looked at two sets of sequential beam test runs taken respectively on December 2013 and March 2014. The runs I looked at for December were taken as the system was warming up, while the runs I looked at for March were taken during a measurement with the system already warmed up. From these beam test runs I looked at the gaussian pulse height distributions from the DAQ as interpretations of the energy deposition in the five channels of the calorimeter. An example of a raw (no cuts made yet) pulse height distribution is displayed in Fig. 4.1.

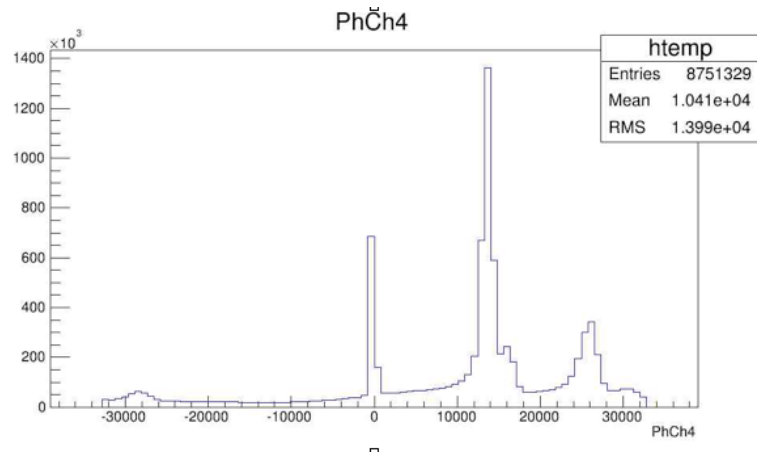


Figure 4.1: STEP 1: This is an example of a histogram displaying an energy detector's (channel 4 in this picture) pulse heights. I look at these histograms for all channels 0-4 for every run I am going to use in my final graph.

The largest most prominent peak in Fig. 4.1 is the relevant effective readout of a proton's residual energy. To quantify this peak, I fitted a Gaussian function to it (after cutting out the rest of the plot that doesn't correspond to the peak) and recorded the values of a fitted mean and sigma. This process was done for all five channels for every beam test run I evaluated in my analysis (both the December and March sets). An example of this fit is displayed in Fig 4.2.

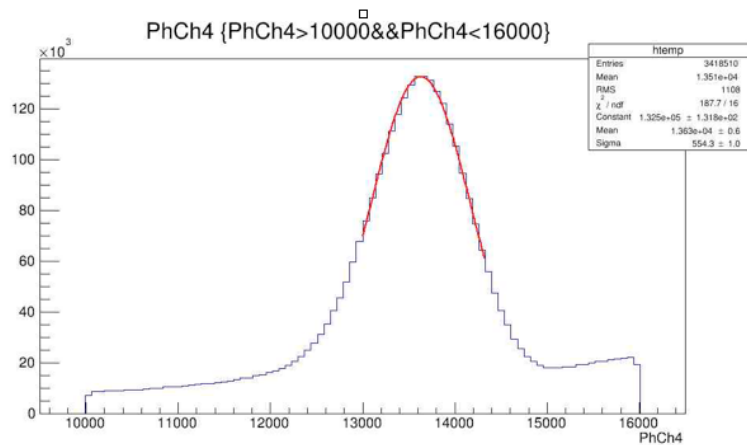


Figure 4.2: STEP 2: This is a gaussian fit being applied to the most prominent (single proton) peak of the histogram from the last slide. I write down the displayed mean/sigma values of this gaussian fit.

The runs for the December beam test I looked at had no phantom while the March beam test runs were taken with a phantom. Since the pulse height distribution for the protons that passed through the phantom does not have a Gaussian shape, I selected events where the proton missed the phantom. An example of the phantom's relative "intrusion" for my analysis is displayed in Fig. 4.3, the purple region indicates the phantom's presence (notice how purple corresponds to a much lower energy deposition, which makes sense since protons that passed through the phantom should have less residual energy than those that did not).

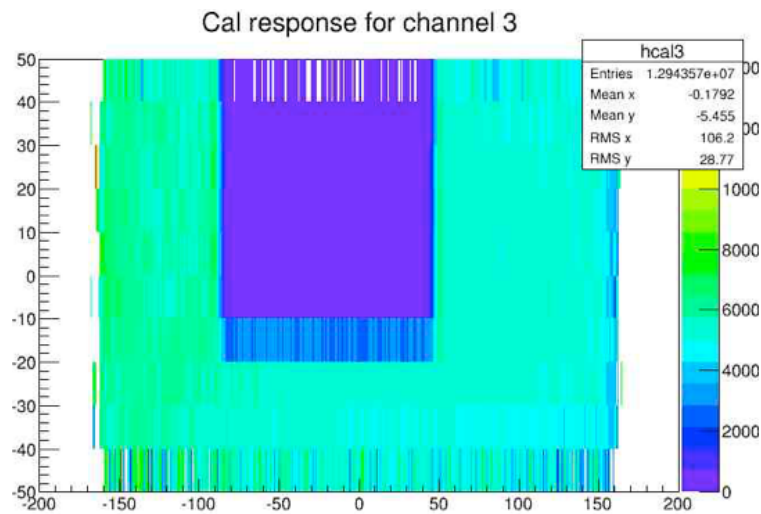


Figure 4.3: STEP 3: This is the scanned image of the water phantom taken from the March beam test. I only used both side areas where the protons completely miss the phantom for the analysis.

With this confounding factor controlled for the March beam test data, I then plotted how the fitted pulse height mean values change over the sequence of runs for both tests, in other words I looked at the proton energy deposition detected as a function of time. The graphs for both the March and December beam test are displayed in Fig. 4.4.

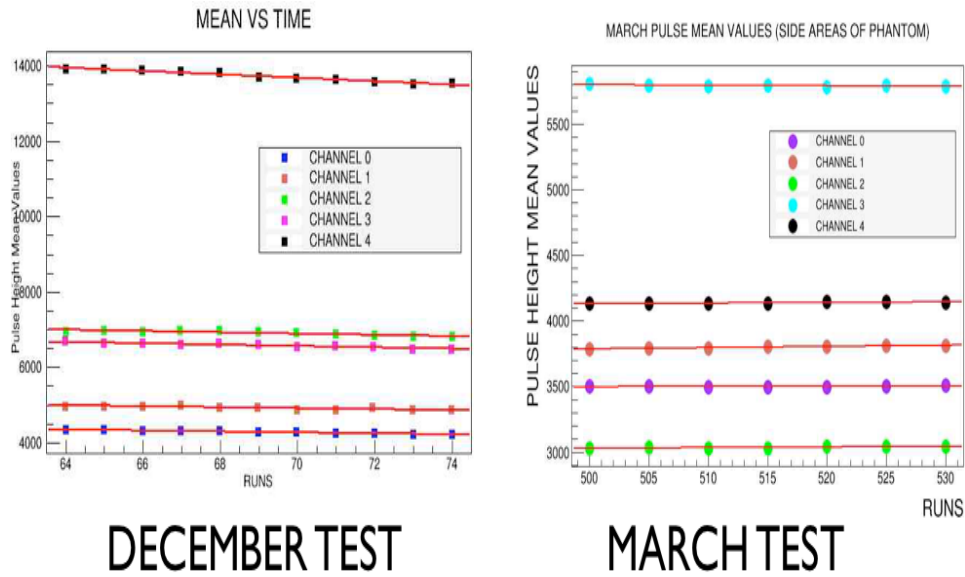


Figure 4.4: STEP 4/finale: With the December test on the left and the March test on the right, we can see the energy detectors pulse heights change systematically over time for the December test, which is when the machine was heating up as the test was running.

The red lines are fitted linear slopes to each channel's curve, the numerical values of these slopes and their respective uncertainties are displayed in Fig. 4.5.

December Beam Test Slopes

CHANNEL	SLOPE&error
0	-13.45 (+/- 1.16)
1	-14.96 (+/- 1.47)
2	-17.8 (+/- 2.34)
3	-19.46 (+/- 0.90)
4	-44.87 (+/- 3.37)

March Beam Test Slopes

CHANNEL	SLOPE&error
0	0.15 (+/- 0.12)
1	-0.01 (+/- 0.23)
2	0.20 (+/- 0.17)
3	-0.35 (+/- 0.36)
4	0.29 (+/- 0.16)

Figure 4.5: STEP 4/finale: Notice the slopes for the March Beam Test are extremely close to zero or contain zero in their interval of error relative to the slopes for the December Beam Test. The non-small magnitude in all the slopes for the channels in the December Beam Test indicate there is a noticeable change in the pulse height over time as the machine is warming up

Every channel for the December beam test has non-negligible slopes while every channel for the March beam test has virtually negligible slopes. Since the runs from the December beam

test correspond to when the scanner was warming up, it appears the energy detectors do have a temperature dependence. Robert Johnson mentioned a possible mechanism at work for this apparent temperature dependence could be the thermal expansion of the photo-multiplier tubes from the temperature increase. In accordance with my results and Professor Johnson's thoughts, I speculate that maybe the altered geometry of the photo-multiplier tubes from thermal expansion could possibly have a relation to the apparent decrease in energy detection as a function of time (and implicitly a function of temperature) displayed in the December test plot of Fig. 4.4.

5 Efficiency of the Track Reconstruction

Algorithm

Although there are gaps within the tracking boards that an incident proton can go through and thus go undetected, the relative offsets of the boards can result in the detection of a gap-passing proton further downstream. With knowledge of a proton's trajectory coordinates on ideally three of the four tracking boards, a geometric algorithm within the preprocessing code can reconstruct a proton's travelled path. This reconstructed track will intersect the tracking board that the proton missed (because it travelled through a gap); a consequence that results in lost data being recovered. Great, but how close does this reconstructed track actually intersect with the exact point of passage within a gap, how efficient is the geometric algorithm? The following analysis is an attempt to quantify the efficiency of track reconstruction by creating artificial gaps within the first tracking board's T layer for events that don't have any missed hits within any of the tracking boards. The reason these events are chosen is so that I can have a reference point of where a proton hit (look up `italicize command`)[should] horizontally be within the plane of the first tracking board's T layer. I created a single gap within each of the first T layer's four sensor boards and analyzed these respective gaps independently. The relative orientation of these gaps is displayed in Fig. 5.1.

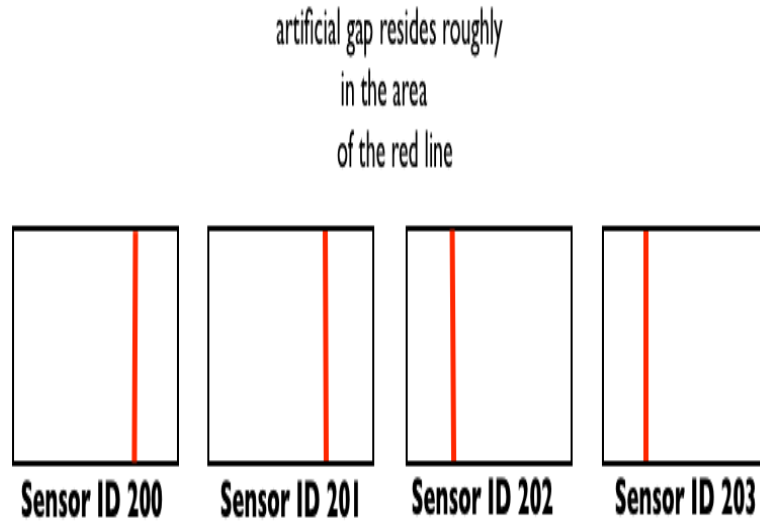


Figure 5.1: This figure displays the first T layer and the relative orientation of the artificial gaps I created.

The way I defined these artificial gaps in the preprocessing code was the removal of four adjacent silicon strip detectors, resulting in a created gap of width of 220 micrometers. I will now walk through the analysis of one sensor board's artificial gap recovery as the process for the remaining three artificial gaps are identical. The sensor I chose for this walkthrough was sensor ID 202, Fig. 5.2 displays the detected hit distribution of the first T layer with the artificial gap created in sensor ID 201 before and after the geometric algorithm was applied.

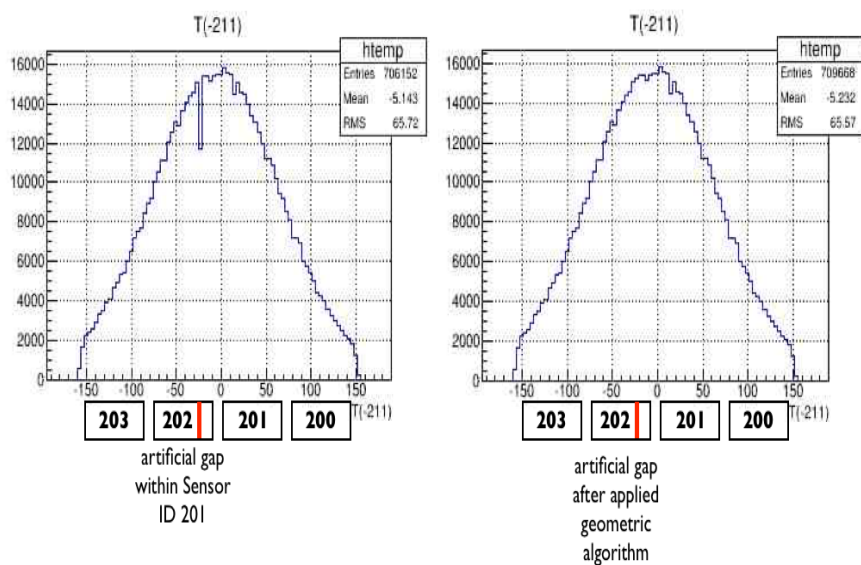


Figure 5.2: These are the raw T-Board layer 0 distributions, as you can see, on the left is the artificial gap I created, and on the right is the successful work of the geometric algorithm generating artificial hits for this gap; effectively filling it. Being that this sensor board is on a far side not as close to the incoming beam, there is less hits to work with so the artificial gap in the position distribution is noticeable smaller..... notice how the sensors are flipped, the reason for this is beyond my knowledge.

A closer look at the distribution of the artificial gap region before and after the geometric algorithm was applied is displayed in Fig 5.3.

T BOARD LAYER 0: SENSOR 202

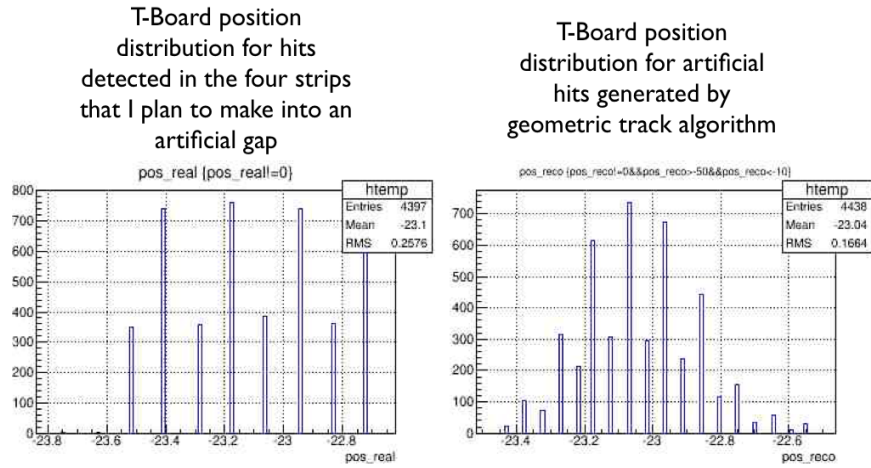


Figure 5.3: These are the raw T-Board layer 0 distributions for the specific gap regions. On the left is the real hit distribution before it was removed to create an artificial gap and on the right is the recovered/artificial hit distribution created by the geometric algorithm. generating artificial hits for this gap; effectively filling it.

Subtracting the real hit T-position distribution from the artificial hit T-position distribution (both displayed in Fig. 5.3) we can get a resulting distribution that one can interpret as how accurate were the positions of these missing hits reconstructed. I fitted a gaussian curve to this distribution and obtained $\sigma_{reco} \approx 172$ microns, the distribution is displayed in Fig. 5.4.

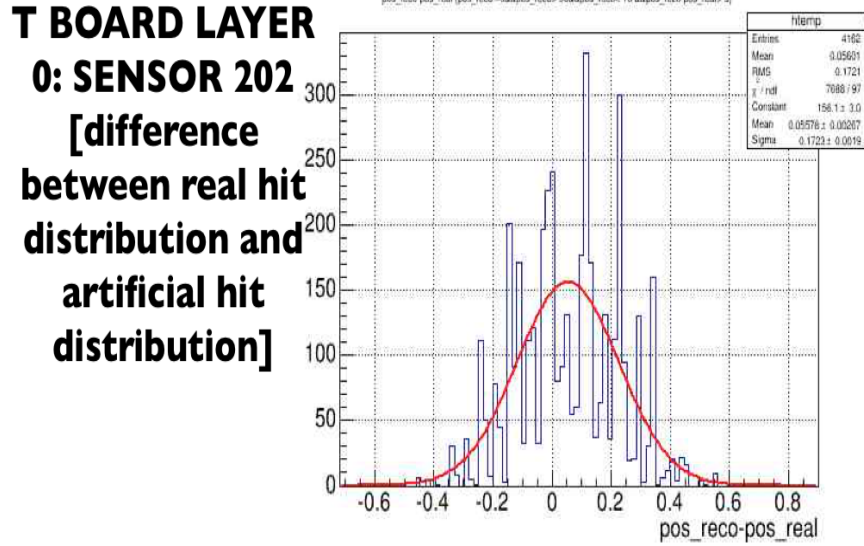


Figure 5.4: This figure displays the resulting distribution of taking the difference between both distributions displayed in Fig. 5.3

The active area of single strip detector is 220 microns, thus assuming a uniform distribution the uncertainty (sigma) of a real hit's position is:

$$\sigma_{real} = \pm \frac{220}{\sqrt{12}} \mu m \approx \pm 66 \mu m$$

The reason the active area is divided by $\sqrt{12}$ is explained in Appendix B. With a repeat process of analysis for Sensor 202 for the other three sensors in T layer 0, I can summarize my results in Fig. 5.5.

	Sensor ID 200	Sensor ID 201	Sensor ID 202	Sensor ID 203
ERROR OF RECOVERED HIT POSITIONS	+/- 181 microns	+/- 172 microns	+/- 172 microns	+/- 180 microns
ERROR OF DETECTED HIT POSITIONS BEFORE THEY WERE REMOVED FOR ARTIFICIAL GAP CREATION				+/- 66 microns

Figure 5.5: This figure displays the resulting σ_{reco} 's I found for every T board's (Layer 0) sensor's created artificial gap as well as σ_{real} for convenient visual comparison.

With knowledge of the real hit's position uncertainty and the recovered hit's position uncertainty we can propagate through a final uncertainty (for Sensors 201 and 202) of :

$$\sigma_{final} = \sqrt{\sigma_{reco}^2 - \sigma_{real}^2} = \sqrt{(172\mu m)^2 - (66\mu m)^2} \approx \pm 160\mu m$$

(increasing from +/- 66 microns before the recovery algorithm) for sensors 201 and 202 (sensors 200 and 203 are on the order of this result although since they were further from the incoming beam there was less hits/statistics to work with so their errors aren't as accurate). Regardless, it seems the track recovery algorithm is able to recover a T-board layer 0's hit position within a factor of 3 of it's original uncertainty.

6 Analytic Determination of Dose

When energy is deposited within a medium via radiation, one can quantify this interaction as an absorbed dose which can be calculated as the total energy deposited within a defined medium's volume divided by the mass of that volume. An ionization chamber is a device that can be used to detect an absorbed dose. When an accelerated proton passes through an ionization chamber, it may have radiation interactions within this chamber's medium in such a way that the atoms of this chamber's medium will be ionized. This ionized charge can be collected by some kind of anode device belonging to the chamber's structure where a mathematical calculation can then be done to interpret an absorbed dose from the incident proton that passed through. In this way, a quantitative estimation of an absorbed dose from a pCT scan can be measured with an ionization chamber placed in a phantom for medium contrast. This measurement process was done during a beam test run from the December 2015 beam test taken at the Northwestern Medicine Chicago Proton Center's cyclotron, the specific 6 minute scan I will be analyzing was done for a cylindrical acrylic phantom with the ionization chamber placed in the middle of it.

To gain a new understanding of the accuracy of the pCT scanner's data acquisition abilities, I attempted to estimate the dose of radiation detected by the ionization chamber for the entire scan by looking at an event distribution that requires a TV plane constraint of a square centimeter extrapolated to $U = 0$ (center of ionization chamber inside middle of acrylic phantom). I then plotted a distribution of all super tracks that were able to pass through this square cm constraint for the entire run's duration, the amount of super tracks in this distribution can then be interpreted

as a planar fluence. To build a correct equation for the planar fluence, I will define the following variables:

The number of super tracks in this distribution for the December beam test run which I will refer to as File D was found to be 29,443 for the first 10 million events of the file. File D contains $N = 330,443,372$ events but it would have taken a very long time to plot the previously stated distribution for the entire file, so instead I made I looked at the first 10 million via the assumption (given by Professor Robert Johnson) that the super track behavior does not change for the remaining events of the file. So, I will define the following variable:

n = number of super tracks in square cm constraint for first 10 million events of File D = 29,443

There are two efficiency factors that need to be attached to this super track total, the first one known as the live-time factor will be defined as the following:

live-time = τ : The run lasted 6 minutes and had 330,443,372 events from 339,898,521 triggers: $\tau = \frac{330,443,372}{339,898,521} = 0.9722\%$

The second factor known as the super track efficiency factor will be defined as the following:

super track efficiency = ϵ_S : Professor Robert Johnson's efficiency program when ran for the first five million events of File D results in 260540 events with at least 1 V and 1 T hit in the central region of the front tracker, and of those events, only 201541 have a super track, the super track efficiency is then $\epsilon_S = \frac{201,541}{260,640} = 0.774$

I am now ready to define my equation for the planar fluence Φ of my square cm constraint:

$$\Phi = \frac{N \cdot n}{\tau \cdot \epsilon_S} \quad (6.1)$$

Plugging in the stated values of N , n , τ , ϵ_S into Eq. 6.1, I was able to calculate a planar fluence of $\Phi = 1,294,598$ protons. Great, but now I would like to know how much the total summed deposited energy is of all the protons Φ deposits after traveling 1 cm past the square cm constraint because doing so would create a cubic cm of energy deposition that will get me one step closer

to a dose calculation. I calculated this total energy using the PSTAR program developed by the National Institute of Standards and Technology (NIST) [7] to find out how much energy each proton should have lost from traveling through 1.6mm of silicon (the first two TV tracker boards), 7.5 cm of acrylic (the radius of phantom before ionization chamber), and finally 1cm of water inside the chamber to interpret a water equivalent dose (chamber doesn't really contain water). The result and conceptualization of each of these energy depositions through the apparatus is displayed in Fig. 6.1

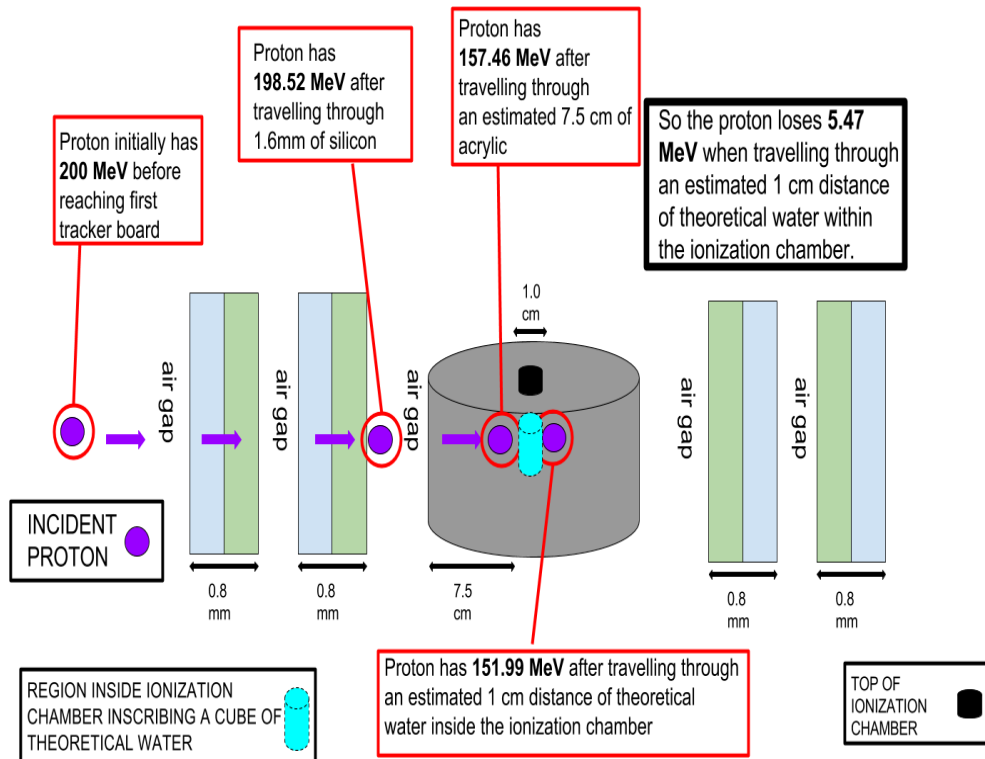


Figure 6.1: This figure displays the path of a single accelerated proton that travels through my square cm constraint as well as the amount of energy this proton loses/deposits through the various mediums of the pCT scanner apparatus.

The concluding result to Fig. 6.1 is that one proton deposits about 5.47 MeV in a 1cm traveled distance through theoretical water inside the ionization chamber. Multiplying this 5.47 MeV energy loss from each of the protons by all the protons in my square centimeter region gives me a total energy deposition in a roughly cubic cm region inside the chamber. That total deposition amounts to $E_{tot} = \Phi \cdot 5.47 \text{ MeV} = 7,081,451 \text{ MeV}$. With this calculated total energy deposition

in a square cm cross section integrated (using PSTAR) over a 1cm distance I can now estimate an analytically calculated absorbed dose D_A received in this cubic cm region by dividing E_{tot} by the mass of a cubic cm of water m_w :

$$D_A = \frac{E_{tot}}{m_w} \approx 1.13 \cdot 10^{-3} \frac{J}{kg}$$

Therefore my final result is a calculated analytical dose of about 1.13 mGy. The ionization chamber located at the same region (visible in the center of the phantom of Fig. 6.1) I calculated my dose for measured a dose of about 1.40 mGy. I believe the reason for the discrepancy between the measured value and my calculated value has to do with my assumption of straight line proton trajectories through my fluence region. Assuming scattering events actually took place within the phantom during the scan, the numerical value of my fluence calculation would be inaccurate and thus result in a distortion of my dose calculation. Via the measurement value being higher than my calculated value, I speculate that there were many curved trajectories outside my square fluence region that still made their way into the cubic dose volume further downstream inside the 1 centimeter depth constraint of the cubic volume. In other words, I assumed no curved proton trajectories made their way into my fluence constraint within 1 centimeter downstream from where this constraint was defined, this assumption may have been an inaccurate one judging by the discrepancy between my calculated dose and the measured dose.

7 Conclusion

After characterizing the preprocessing code for the pCT DAQ it appears Steps 3 and 5 are the most responsible for the loss of data to be used for potential image reconstruction while Step 2 is the least responsible. Via the investigation of a beam test run taken while the energy detectors were warming up compared with a beam test run taken while the energy detectors were in essentially systematic thermal equilibrium, it appears the calorimeter does have a temperature dependence. Using created artificial gaps, the track reconstruction algorithm increases the hit position uncertainty by about a factor of 3 for the T layer of the first tracking board. By making a square cm fluence constraint extrapolated at $U = 0$, I was able to calculate an analytical approximation to a water equivalent absorbed dose of about 1.13 mGy for a 6 minute scan. This calculation has a discrepancy with the measured value (with an ionization chamber) of 1.40 mGy, I believe the difference between these values is mostly due to assuming straight line proton trajectories through my fluence region when realistically some of the proton trajectories may have been curved due to scattering events. Therefore, these curved trajectories may have entered my cubic dose volume somewhere within 1 centimeter downstream of my defined constraint region which would result in a higher dose measured by the ionization chamber compared to my calculation.

Appendix A The Possibilities of Step 1

To further characterize every possible type of event Step 1 can reject in **Section 3.1**, I will start with the following definitions:

Def 1. 1 = at least one hit within respective layer pair of a tracking board

Def 2. 0 = no hits within respective layer pair of a tracking board

With these definitions, Table A.1 outlines the $2^4 = 16$ types of events rejected from Step 1 as well as the amount of events rejected from each case for File P:

Table A.1: This table displays every possible case of tracker board hit combination that can cause an event to fail Step 1.

CASE TYPE	# OF EVENTS REJECTED (FOR FILE P)
1110	18498
1101	15680
1100	10552
1011	22697
1001	580
1000	6535
1010	42910
1111	17833
0100	10973
0110	810
0101	169081
0111	0
0011	12241
0010	13998
0001	18102
0000	406432

Appendix B Justifying $\sqrt{12}$

In Chapter 5 after assuming a uniform distribution for the active area of the strip, I claim the hit position uncertainty on that strip is the active area divided by $\sqrt{12}$, let's justify why. Let $f(x)$ represent the probability density function (if you integrate it over $b-a$ you will calculate 1) between the width of my strip which I will define as $b-a$.

$$f(x) = \frac{1}{b-a} \quad \text{for } a < x < b$$

[$f(x) = 0$ for everywhere else outside of the active area of the strip]

So, recall that the standard deviation formula is of the form (mean of square minus square of mean) displayed in Eq. B.1.:

$$\sigma = \sqrt{E[x^2] - (E[x])^2} \tag{B.1}$$

The expectation value of the mean position of x can be calculated the following way:

$$E[x] = \int_a^b \frac{x \cdot dx}{b-a} = \frac{1}{b-a} \left[\frac{x^2}{2} \right]_a^b = \frac{1}{b-a} \left(\frac{b^2}{2} - \frac{a^2}{2} \right) = \frac{(b+a)(b-a)}{2(b-a)}$$

$$E[x] = \frac{b+a}{2}$$

Therefore the expectation value of the mean squared is given by Eq. B.2:

$$(E[x])^2 = \frac{b^2 + 2ab + a^2}{4} \tag{B.2}$$

The expectation value of the squared mean can be calculated the following way:

$$E[x^2] = \int_a^b \frac{x^2 \cdot dx}{b-a} = \frac{1}{b-a} \left[\frac{x^3}{3} \right]_a^b = \frac{1}{b-a} \left(\frac{b^3}{3} - \frac{a^3}{3} \right) = \frac{(b-a)(b^2 + ab + a^2)}{3(b-a)}$$

Therefore the expectation value of the squared mean is given by Eq. B.3:

$$E[x^2] = \frac{b^2 + ab + a^2}{3} \tag{B.3}$$

Plugging in Eq. B.2 and Eq. B.3 into Eq. B.1 we have:

$$\sigma = \sqrt{\frac{b^2 + ab + a^2}{3} - \frac{b^2 + 2ab + a^2}{4}} = \sqrt{\frac{4b^2 + 4ab + 4a^2 - 3b^2 - 6ab - 3a^2}{12}}$$

$$\sigma = \sqrt{\frac{b^2 - 2ab + a^2}{12}} = \sqrt{\frac{(b-a)^2}{12}}$$

Thus we have arrived at the standard deviation formula for a uniform distribution.

$$\sigma = \frac{b-a}{\sqrt{12}} \tag{B.4}$$

Since b-a is the active area of my strip, Eq. B.4 justifies my claim that the hit position uncertainty for a strip is it's active area divided by $\sqrt{12}$.

Bibliography

- [1] https://www.medphysics.wisc.edu/courses/mp501/501_lecture1.pdf
- [2] E.B. Podgorsak, "Radiation Oncology Physics: A Handbook for Teachers and Students".
September 2005.
- [3] <http://mynameishalo.deviantart.com/art/Atomic-Collision-3-124245003>
- [4] "Exploring the Benefits of Proton Therapy." Proton Therapy Side Effects. N.p., n.d. Web. 07
Feb. 2016. <https://www.floridaproton.org/what-is-proton-therapy/benefits>.
- [5] "History of Proton Therapy." N.p., n.d. Web. 23 Jan 2016.
<https://www.mdanderson.org/patients-family/diagnosis-treatment/care-centers-clinics/proton-therapy-center/what-is-proton-therapy/history-of-proton-therapy.html>
- [6] Robert P. Johnson, *et al.*, "A Fast Experimental Scanner for Proton CT: Technical Performance and First Experience With Phantom Scans"
- [7] <http://physics.nist.gov/PhysRefData/Star/Text/PSTAR.html>